1993ApJ...409...91H

THE ASTROPHYSICAL JOURNAL, 409:91–109, 1993 May 20

GALACTIC BARS WITH CENTRAL MASS CONCENTRATIONS: THREE-DIMENSIONAL DYNAMICS

HASHIMA HASAN
Space Telescope Science Institute, Baltimore, MD 21218
DANIEL PFENNIGER
Observatoire de Genève, CH-1290 Sauverny, Switzerland
AND
COLIN NORMAN
Department of Physics and Astronomy, Johns Hopkins University, Baltimore, MD 21218;
and Space Telescope Science Institute, Baltimore, MD 21218[1]
Received 1992 June 5; accepted 1992 November 18

ABSTRACT

The stellar dynamics at the transitions between a strongly barred and rotating potential and a spherical and dense central mass concentration is investigated in a model potential. Three different degrees of concentration of the central mass are studied. The main families of three-dimensonal periodic orbit are found by numerical means. The structure of phase space is presented by bifurcation diagrams and surfaces of section. A large region of instability develops near the inner Lindblad resonance (ILR) due to the strong bar potential. In such a mass configuration the radial ILR is typically near the corresponding vertical ILR, consequently the instability of orbits is radial as well as vertical, helping the heating of disk stars into a bulge. These secular evolution processes from barred to unbarred and in the direction of increasing the bulge-to-disk ratio should affect the evolution of galaxies over a Hubble time.

Subject headings: celestial mechanics, stellar dynamics — galaxies: evolution —
galaxies: kinematics and dynamics — galaxies: nuclei

1. INTRODUCTION

The structure of barred galaxies seems to exhibit a number of subtleties that require further elucidation, including the questions of why only ~30% of all galaxies have a detected strong bar, why polar rings are not found in barred galaxies (Bettoni & Galletta 1991), and whether galaxies can evolve through bar dissolution to ovals or lenses (Kormendy 1979, 1982). In a recent study (Pfenniger & Norman 1990) it was found that barred galaxies with significant central mass concentrations could resonantly heat disk stars sufficiently strongly to populate a metal-rich rapidly rotating bulge, which, in the Milky Way and nearby galaxies, is indeed observed (Mould 1986; Frogel 1988; Rich 1989). ("Bulge" here is as defined by Gilmore, Wyse, & Kuijken 1990 and is really the inner, ~3–5 kpc wide bulge as opposed to the more extended spheroid.) In this regard, the tendency of N-body bars to develop into box- or peanut-shaped bulges when seen on edge (Combes & Sanders 1981; Combes et al 1990) is to be connected with the boxy near-infrared view of the Milky Way bulge (Hayakawa et al. 1981; Habing et al. 1985; Kent et al. 1992). In the N-body models the development of the peanut shape is due to a vertical 2:1 instability of the plane orbits which triggers a z-asymmetric gravitational bending mode, as studied for barred systems by Pfenniger & Friedli (1991) and Raha et al. (1991). During the formation of this peanut-shaped bar-bulge there is a substantial heating parallel and normal to the plane and a corresponding increase of its central density. Since the gravitational bending instability is then global to the bar, though initiated by an orbital resonance, it is more effective than just a resonant instability restricted to localized regions in space.

A detailed theoretical study of stellar orbits in rapidly rotating triaxial galaxies in the presence of a central mass concentration is an important step in understanding the shapes and secular evolution of such galaxies, as well as in constructing self-consistent models of the galaxy potential (Schwarzschild 1979, 1982; Pfenniger 1984b). A first approach to this problem was made in an earlier paper (Hasan & Norman 1990, hereafter Paper I), where we examined the two-dimensional behavior of the orbits in the galactic plane as the central mass grew in mass. We found that as the central mass became larger the B (or x_1) family of orbits (in the notation of Athanassoula et al. 1983), which are the ones elongated along the major axis of the bar and which are important in sustaining the bar, became more and more unstable, and therefore surrounded by stochastic orbits, until eventually the bar had to dissolve. This behavior was associated with the appearance of an inner Lindblad resonance (ILR) which gradually moved toward the minor axis of the bar. An estimate of stochasticity was made by computing the volume in phase space occupied by the stable B orbits. As the central mass concentration was increased, the phase-space volume decreased down to zero.

The perhaps overly ambitious hypothesis that has emerged from these studies so far is that all galaxies tend to be barred but the bar acts to sweep material into a central mass concentration that then acts to dissolve the bar. At the same time, considerable disk heating is occurring and the central bulge (the inner bulge, not the spheroid) is forming or being added to significantly. These slow secular processes ($\tau \simeq 10^9$ yr) can be thought of as acting to transform galaxies from one type to another from barred to unbarred and in the direction of increasing the bulge-to-disk ratio. Of course, other physical processes are also occurring, including star formation and

---

[1] Postal address.

1993ApJ...409...91H

merging of both large and small objects, but here we will focus on these slow secular continuous processes. Interesting attempts at N-body work along these lines (Friedli, Benz, & Martinet 1991; Pfenniger 1991, 1983; Friedli & Benz 1993) show bar dissolution with central buildup of mass either by gas accretion or by satellite merging.

Analyzing such self-gravitating systems completely is enormously difficult owing to the large number of degrees of freedom in interplay. In fact, typical N-body systems are exponentially unstable and therefore generate much more chaos than is classically expected from Chandrasekhar's two-body relaxation estimate (Gurzadayan & Savvidy 1986). As a consequence, individual orbits in self-consistent N-body calculations do not conserve their assumed integrals of motions well and are "relaxed" much faster than by two-body encounters. So either the approach to model galaxies based on the collisionless Boltzmann equation or the one based on studying orbits in a fixed galactic potential has a limited scope of application in actual galaxies and in N-body numerical systems. The fact that the notion of an integral of motion is valid only for a restricted time scale ($\approx 10^8$ yr) is also well documented observationally in the Milky Way by the systematic increase of the star velocity dispersion with age in both the radial and vertical directions (Wielen 1977).

However, recognizing that the most robust structures of phase space (after the equilibrium points) in a galactic potential are the major periodic orbits (Pfenniger 1992), we shall use here single-particle orbits in given potentials, hoping eventually to achieve sufficient insight to attack the study of N-body models. The importance of stable periodic orbits is, first, that they form the underlying basis for the dynamical description of phase space, since they summarize the six-dimensional single-particle phase space, and, second, that they *survive* for much longer times to conservative and dissipative perturbations than other orbits. So even if the potential adopted below is approximate or, if perturbative, conservative, or dissipative forces are neglected, the basic motion in a real barred galaxy with a central mass concentration has to be qualitatively similar, for several orbital periods, to the one described in this study.

The analysis of the problems discussed above could generate many papers, but the problem we focus on here is that of classifying the main periodic orbits for a three-dimensional barred potential containing a central mass. In a previous work (Pfenniger & Norman 1990) it was shown that for typical galactic setups, a 2:1 vertical resonance in the galactic plane and within the corotation radius cannot be avoided for direct motion when the potential goes from spherical to flattened. Therefore, the configuration studied is generic to barred galaxies with a central mass concentration, where the potential is spherical at the center and is flattened outside the corotation radius that is close to the bar end, and the resonances are widened by the important bar perturbation. The two-dimensional problem has been studied by Hasan & Norman (1990) for the rapidly rotating bar. The orbits in a nonrotating elliptical galaxy with a central density cusp has been studied by Miralda-Escudé & Schwarzschild (1989), Martinet & Udry (1990), and Udry (1991).

The principal qualitative conclusions of this work are that the central mass concentration will dissolve the bar, consistent with the previously studied two-dimensional case (Paper I), and that vertical resonances could lead to heating of the disk normal to the plane. The retrograde and anomalous orbit families, since they avoid the central region, remain stable.

In § 2 we describe the potential used. In § 3 we study the motion in the plane, and in § 4 we describe the motion outside the plane, giving orbit analysis and bifurcation diagrams where possible. Section 5 summarizes the principal conclusions.

2. POTENTIAL MODEL

Previous studies of barred galaxies (Athanassoula et al. 1983; Pfenniger 1984a) have shown us which parameters well characterize the bar region of a barred galaxy in an approximate, but tractable, galaxy model. Retrospectively, even crude mass models (e.g., Contopoulos & Papayannopoulos 1980) with negative density parts (cf. Petrou 1984) are perfectly able to reproduce the main families of periodic orbits. As mentioned in § 1, this is due to the fact that periodic orbits are the most robust structures of phase space.

The choice of the potential parameters and pattern speed are derived from previous studies (Pfenniger 1984a, b), where the orbits of a similar barred galaxy model were considered and shown to be able to reproduce the density model in a self-consistent way (in two dimensions only). The main difference here is the introduction of a spherical central mass of tunable concentration.

Accordingly, the galactic potential is approximated by

$$\Psi = \Psi_c + \Psi_b + \Psi_{\rm cm} , \tag{1}$$

where Ψ_c and $\Psi_{\rm cm}$ represent the disk and central mass concentrations, respectively. The disk is modeled as a Miyamoto disk:

$$\Psi_c = -\frac{GM_c}{\{R^2 + [A_c + (B_c^2 + z^2)^{1/2}]^2\}^{1/2}} . \tag{2}$$

Here A_c and B_c are the parameters determining the shape of the disk, G is the gravitational constant, and M_c is the total mass of the sphere. The central mass concentration is represented by a Plummer sphere, which is a special case of the above potential with $A_c = 0$. An inhomogeneous triaxial Ferrers bar with density distribution

$$\rho = \begin{cases} \rho_0(1 - m^2)^2 & \text{if } m < 1 , \\ 0 & \text{if } m \geq 1 , \end{cases} \tag{3}$$

where

$$m^2 = \frac{x^2}{a^2} + \frac{y^2}{b^2} + \frac{z^2}{c^2} , \tag{4}$$

with $a > b > c$, is chosen to model the component Ψ_b of the potential.

The potential parameters are chosen to have values close to the "main" model of Pfenniger (1984a), the principal differences being due to the additional central mass concentration: $GM_b = 0.075$, $b/a = 0.25$, $c/a = 0.1$, $a = 6$, $GM_c = 0.915$, $A_c = 3$, $B_c = 1$, $GM_{\rm cm} = 0.01$, $B_{\rm cm} = 0.1$, 0.01, or 0.001. We choose to modify $B_{\rm cm}$ rather than $GM_{\rm cm}$ in order to mimic an increase of the central mass concentration at constant total mass within the corotation radius.

The bar rotation speed Ω_p is such that the corotation radius $R_{\rm CR}$ lies at the end of the bar major axis a, fixing the rotation speed of the bar, $\Omega_p = 0.05471$. It should be noted that a, the major semiaxis of the Ferrers model, is the extreme distance beyond which the density is axisymmetric, while a typical bar length as derived from observation would be the characteristic bar length, shorter than a by 10%–20%.

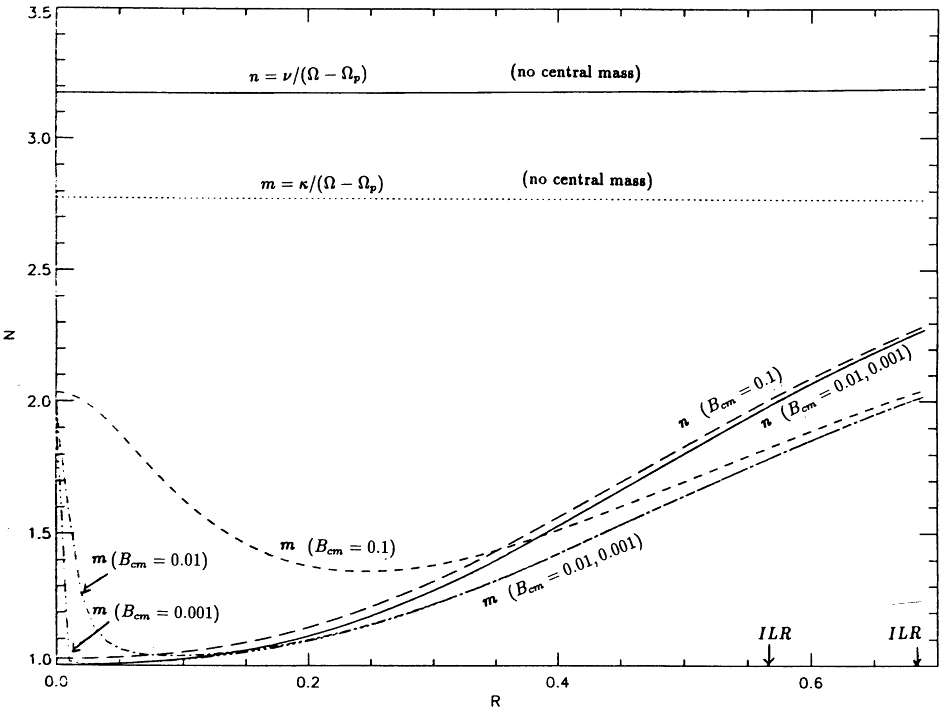

FIG. 1.—Ratios of the radial and vertical epicyclic frequencies to the excitation frequency. An ILR occurs when this ratio equals 2.

With $G = 1$, a convenient set of units is 1 kpc for length, $2 \times 10^{11}\ M_\odot$ for mass, and ~ 1 Myr for time. Hence the velocity unit corresponds to about 1000 km s^{-1}.

The Hamiltonian (Jacobi integral), H, is given by

$$H = \tfrac{1}{2}(\dot{x}^2 + \dot{y}^2 + \dot{z}^2) + \Psi(x, y, z) - \tfrac{1}{2}\Omega_p^2(x^2 + y^2) \qquad (5)$$

for the noncanonical variables $(x, y, z, \dot{x}, \dot{y}, \dot{z})$ in the rotating frame of reference, or by

$$H = \tfrac{1}{2}(p_x^2 + p_y^2 + p_z^2) + \Psi(x, y, z) - \Omega_p(xp_y - yp_x) \qquad (6)$$

for the canonical variables (x, y, z, p_x, p_y, p_z), where $p_x = \dot{x} - \Omega_p y$, $p_y = \dot{y} + \Omega_p x$, $p_z = \dot{z}$. For any particular time the momenta p_x, p_y, and p_z are the velocity components in the instantaneous inertial frame parallel to the rotating frame. We shall loosely refer to the value of the integral H as the "energy" of the orbit.

The potential chosen here has no inner Lindblad resonances in the absence of a central mass, as is seen from Figure 1, where we have plotted the ratios of the natural epicyclic frequencies over the excitation frequency, $(\Omega - \Omega_p)$. Here Ω is the circular frequency defined for an axisymmetric potential as $\Omega^2(R) = \Psi_R/R$, where Ψ_R is the first derivative of Ψ with respect to R evaluated at $z = 0$. The radial epicyclic frequency, κ, and vertical epicyclic frequency, ν, are defined respectively as $\kappa^2(R) = (\Psi_{RR} + 3\Psi_R/R)_{z=0}$ and $\nu^2(R) = (\Psi_{zz})_{z=0}$, where Ψ_{RR}, Ψ_{zz} are the second derivatives of Ψ with respect to R and z, respectively. Since these quantities are defined for axisymmetric potentials, we have approximated the bar potential, Ψ_b, for this computation by an oblate potential which has $a = b = 3$ (the geometric mean of a and b). When a central mass is introduced, we see the appearance of an ILR in both the radial and the vertical plane. The radial resonance is at $R \simeq 0.675$, while the vertical resonance is at $R \simeq 0.575$. Since the radial and vertical resonances nearly coincide (as discussed above, this is generic to a spherical central mass concentration) and since the appearance of a low-order resonance such as an ILR is associated in general with a pronounced stochasticity, we expect a destabilization of motion in the galactic plane as well as close to the plane. This chaotic motion in and out of the plane can heat the bulge.

The above axisymmetric resonances are only an approximation of the real resonances in a barred potential. The actual resonances will manifest themselves as gaps in the bifurcations of periodic orbit families described in § 3. The shape of resonances is not limited to a ring, as in weakly perturbed axisymmetric potentials, but follows the shape of the periodic orbits on each side of the resonance gap.

Figure 2 shows the *circular* rotation velocity of the azimuthally symmetrized models with increasingly concentrated central masses. The models having central masses with $B_{\rm cm} \approx 1$ and more can represent late-type galaxy rotation curves, since their rotation curves are almost identically linearly rising, while models with $B_{\rm cm} \approx 0.1$ and less have steeper rotation curves with a "bump" typical of early-type galaxies. In only these models will the effect of a central mass be significant. The models with $B_{\rm cm} \approx 0.01$ or less have a very steep initial rising curve, reaching a high maximum within a small radius, that in usual observations would be unobservable owing to the low systemic rotation of stars in these central regions and also to insufficient spatial resolution.

The equations of motion are solved numerically. The techniques to compute surfaces of section (or Poincaré maps) to determine the initial conditions of periodic orbits are summarized in the Appendices.

3. MOTION IN THE GALACTIC PLANE

We shall analyze the stellar motion by examining the periodic orbits and their "families" supported by the galactic poten-

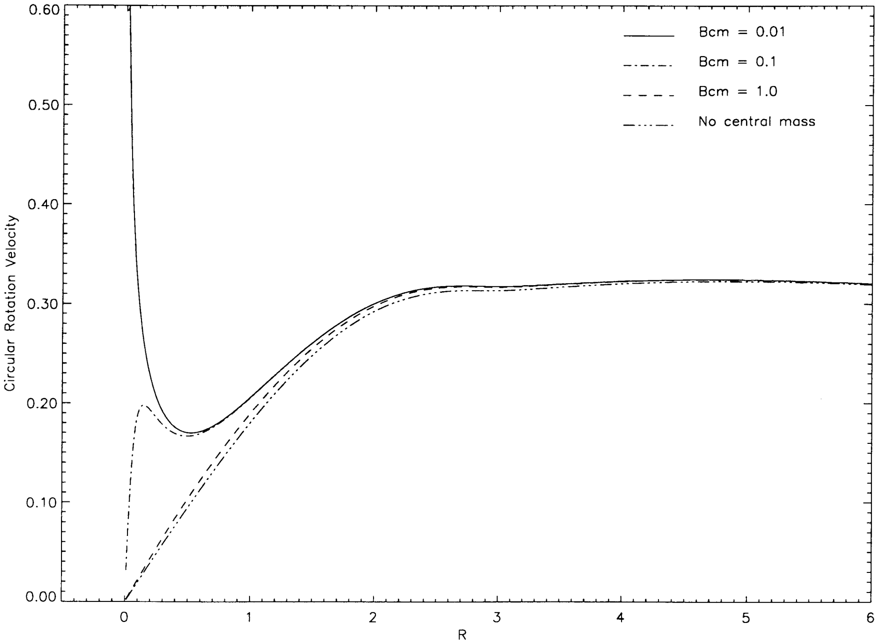

FIG. 2.—Circular rotation velocity in the axisymmetrized models, as the central mass concentration is increased from $B_{\text{cm}} = \infty$ (no central mass) to $B_{\text{cm}} = 0.01$. The interesting regime, examined in this paper, occurs when the rotation curve displays a secondary peak near the center, for $B_{\text{cm}} \ll 1$.

tial. The importance of periodic orbits lies in the fact that not only do they determine the mass distribution and hence the shape of the galaxy, but also they are robust structures that survive finite conservative and dissipative perturbations the longest. In order to see the effect of a central mass concentration on the galactic shape it is therefore important to find its effect on the stability of different orbit families. A convenient way of displaying the regions of existence and of stability of the various orbit families is by computing bifurcation diagrams and surfaces of section. We shall discuss each of these separately.

3.1. *Bifurcation Diagrams*

Bifurcation diagrams or periodic orbit families have been extensively used in galactic dynamics to summarize phase space (e.g., Contopoulos & Papayannopoulos 1980; Athanassoula et al. 1983; Pfenniger 1984a, 1985; Teuben & Sanders 1985; Sparke & Sellwood 1987; Pfenniger & Friedli 1991). While such curves provide a wealth of information to the expert, they can often be bewildering to the uninitiated. It therefore seems appropriate to give a brief qualitative introduction to bifurcation (or characteristic) diagrams and orbital stability in the context of the present discussion.

In three-dimensional space periodic orbits can be uniquely represented by their set of initial conditions (x_0, y_0, z_0, $\dot{x}_0$, $\dot{y}_0$, $\dot{z}_0$). To such a set of initial conditions corresponds a function $H(x, y, z, \dot{x}, \dot{y}, \dot{z})$ that remains constant along the orbit: $H(x_0, y_0, z_0, \dot{x}_0, \dot{y}_0, \dot{z}_0) = H(x(t), y(t), z(t), \dot{x}(t), \dot{y}(t), \dot{z}(t)) = H_0$. If we search for periodic orbits within a potential and plot any one of the starting conditions (x_0, y_0, z_0, $\dot{x}_0$, $\dot{y}_0$, $\dot{z}_0$) against the corresponding H_0, we will find continuous curves, the *characteristics* in this two-dimensional projection of initial conditions. Each characteristic on such a *bifurcation diagram* corresponds to a *family* of periodic orbits.

Hence one glance at such a diagram gives us a complete picture of the dynamical system in terms of the orbits that exist in different regions of phase space. It is customary to search for orbits starting in the galactic plane along one of the axes with a velocity transverse to the axis. In the present study we plot the characteristic diagram (H_0, y_0) for periodic orbits starting on the y-axis with $\dot{y}_0 = 0$ and $\dot{x}_0$ computed from equation (5). The dynamical region to which the orbits are restricted is bounded on the characteristic curve by the "zero-velocity" curve computed from equation (5) by setting the velocities to zero.

Along a family the degree of stability varies continuously, and eventually a stable part becomes unstable. At the transition locus, new families typically *bifurcate*. Different but not exhaustive possibilities of bifurcations in Hamiltonian systems have been described by Hénon (1965). The *main* families are the ones which do not originate on another family of periodic orbits (they can originate at a fixed point of the potential such as the center). The bifurcating orbit takes on the stability characteristic of the original orbit as the energy changes. The orbit usually changes in shape and may even be accompanied by period doubling. Bifurcations play an important role in determining the dynamics of three-dimensional systems (e.g., Contopoulos & Magnenat 1985; Contopoulos 1986), since they herald the creation of new orbit families and are often accompanied by instability and chaos. It is these properties that are of greatest interest to us here.

The initial conditions for the bifurcating orbits may have nonzero values for more than one of the phase-space variables. For example, in our case a bifurcation in $\dot{y}$ means that (H_0, y_0, $\dot{y}_0$) are nonzero and determine the value of $\dot{x}_0$. In this case it is important to draw the bifurcation diagram (H_0, $\dot{y}_0$) as well. In our problem, the only bifurcations that correspond to three-dimensional orbits are the ones in z and $\dot{z}$. There may be further bifurcations off these new families, but we do not consider these higher order bifurcations here, since these orbits influence smaller and smaller regions in phase space and are unimportant in determining the morphology of a galaxy.

Orbital stability is mathematically quantified in terms of "stability indices" (Magnenat 1982 and references therein;

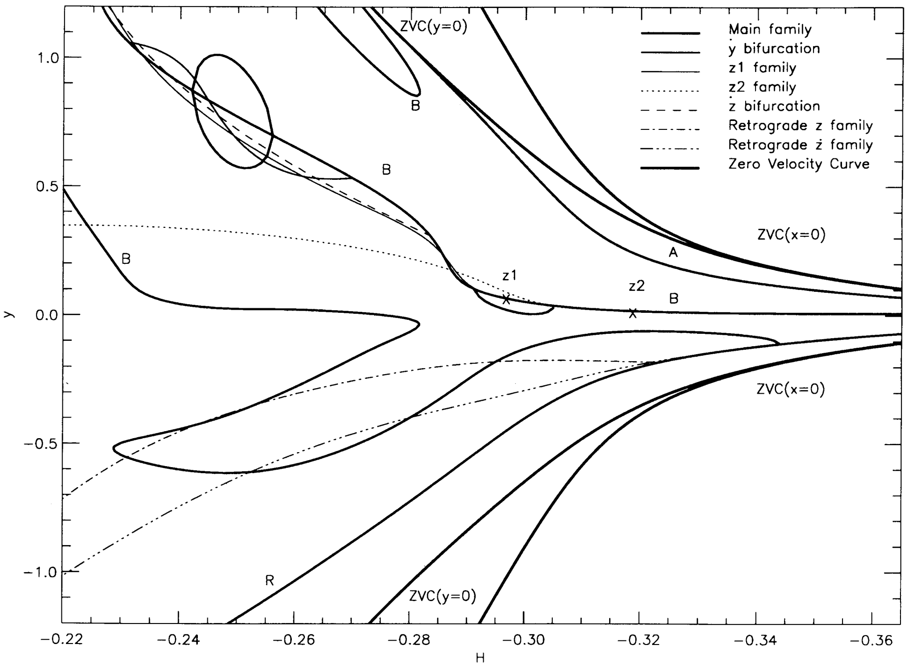

FIG. 3*a*

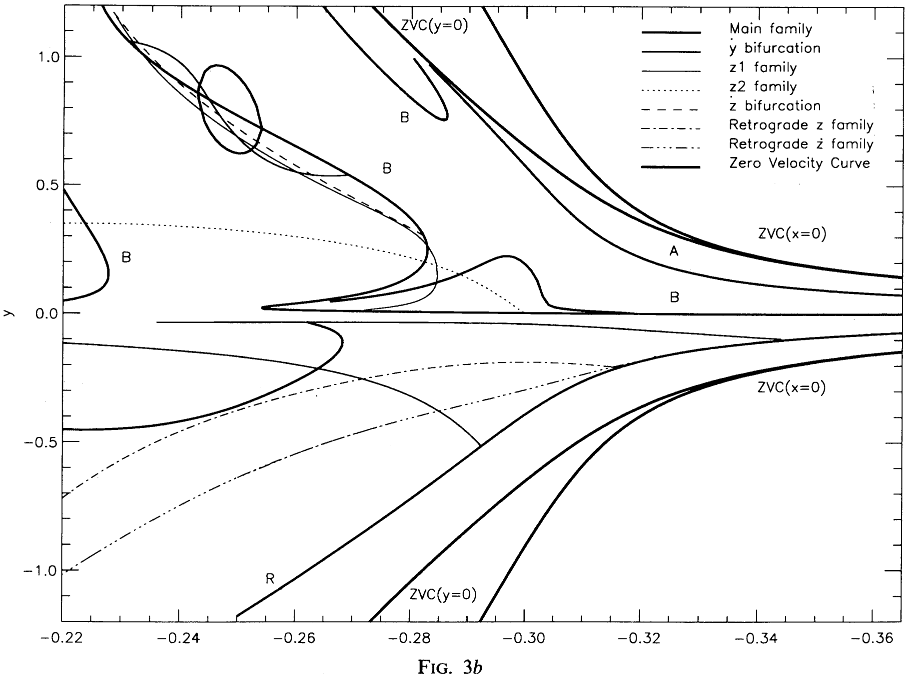

FIG. 3*b*

FIG. 3.—Bifurcation diagrams showing the initial conditions (H_0, y_0) for the main periodic orbit families and their first-order bifurcations for central mass concentrations (*a*) $B_{\rm cm} = 0.1$, (*b*) $B_{\rm cm} = 0.01$, and (*c*) $B_{\rm cm} = 0.001$. The main orbit families are indicated by heavy solid lines, while the bifurcating families are represented by different line types are explained in the key at upper right. The bifurcation points of the $z1$ and $z2$ families for case I are represented by crosses.

1993ApJ...409...91H

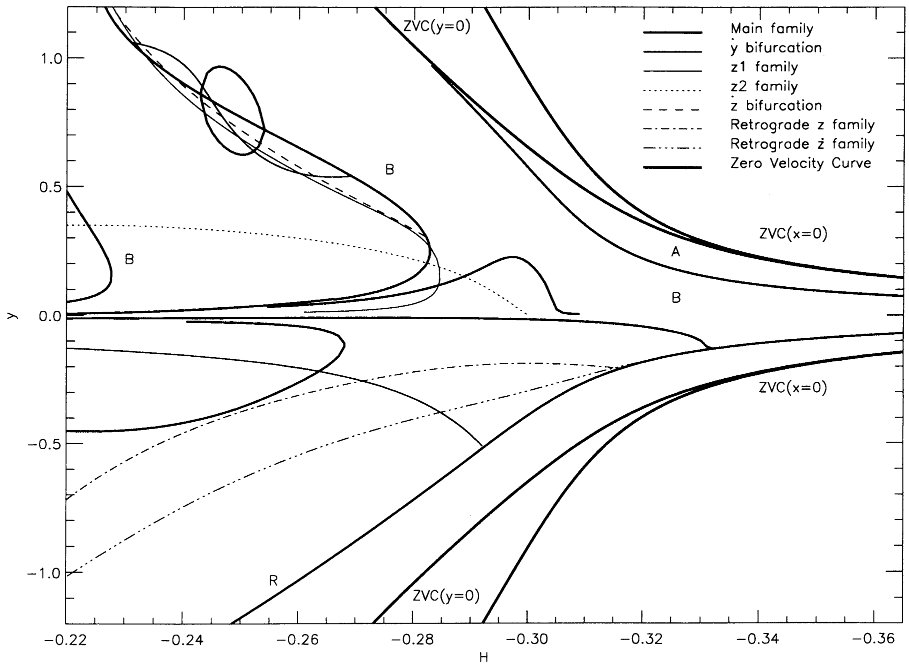

FIG. 3*c*

Appendix B of this paper). These indices have physical significance for orbits in the galactic plane in the sense that they correspond to perturbations transverse to the orbits, either in the orbital plane or at right angles to it. The stability of periodic orbits is broadly classified as *stable*, *simply unstable*, *doubly unstable*, and *complex unstable*. A more refined instability classification due to Broucke (1969) is given in Appendix B. Simply unstable orbits are unstable to perturbations along one fixed direction only, while doubly unstable orbits are sensitive along two fixed directions. Complex instability is a distinct type of instability that appears in autonomous systems with at least 3 degrees of freedom (Broucke 1969). Complex unstable orbits are sensitive to perturbations within a *plane* of rotation in the six-dimensional phase space. The consequents of nonperiodic nearby orbits form a spiral structure in the four-dimensional “surface” of section .Though mathematically well defined, the effect of complex instability is conceptually more difficult to visualize, as a higher than two-dimensional (i.e., four-dimensional) space needs to be considered. This phenomenon, however, has important implications in galactic dynamics (Pfenniger 1985; Martinet & Pfenniger 1987), some of which will be mentioned later in the discussion.

Periodic orbits and their stability indices were computed in the galactic plane by numerically integrating the equations of motion and using a Newton-type method to obtain the initial conditions for the periodic orbits (see Appendices). We shall refer to the three cases considered here as case I ($B_{\rm cm} = 0.1$), case II ($B_{\rm cm} = 0.01$), and case III ($B_{\rm cm} = 0.001$). Characteristic curves are studied for those regions of the bar where the influence of the central mass is expected to be felt.

Bifurcation diagrams for the three cases (Figs. 3*a*–3*c*) show that there are *three major* families of periodic orbits. The first-order bifurcation of these families are also shown. The *three-dimensional periodic orbits* are the ones *bifurcating in z or ż* and will be discussed in § 4. The diagrams are replotted in Figures 4*a*–4*c*, where stable orbits are represented by solid lines, while unstable orbits are represented by broken lines.

A orbits.—These orbits, also called x_2, have an *antibar* shape, so are *elongated perpendicular* to the bar and are more rounded as we go deeper into the potential and are stable along the entire characteristic. They give a round shape to the regions surrounding the central mass concentration, but at larger distance their shape is more and more antialigned to the bar, tending to decrease the eccentricity of the bar.

B orbits.—These direct orbits, also called x_1, support the *bar* because they are mainly *elongated along the bar* and are the most important for bar existence. For case I the corresponding characteristic is smooth and continuous with the orbit evolution shown in Figure 5. We see that while these orbits are elliptical at large energies, as we get close to the central mass they develop loops at the ends. For cases II and III the characteristics are repelled strongly from the interior regions of the bar, with larger regions of instability. In the inner regions of the bar, stable, almost axial orbits exist for case I between $H = -0.35$ and $H = -0.315$, while for case II this region shrinks to $H = -0.35$ to -0.33, disappearing completely for case III. Alternating regions of stability and instability occur all along the characteristic as the energy increases and starting conditions for the periodic orbits move farther from the interior of the potential along the bar intermediate axis, y.

Birfurcations of the B orbits in y and $\dot{y}$.—There are several bifurcations off the main family. The bifurcation in y which forms a bubble (between points 1 and 2 in Fig. 6) contains orbits which are largely oval and elongated along x but are slightly stretched along the y-axis. The orbits *bifurcating in* $\dot{y}$ (between points 3 and 4) form a loop along the x-axis at one end.

Minor families of orbits.—There is one minor family of *largely unstable 3:1 direct orbits*. One section of the characteristic was found near the A family (Figs. 3*a* and 3*b*), and the symmetric counterpart was found crossing the y-axis on the characteristic plot at smaller values. The corresponding characteristic curve for case I (Fig. 3*a*) is found between $H = -0.22$ and $H = -0.28$. At this point the characteristic continues onto

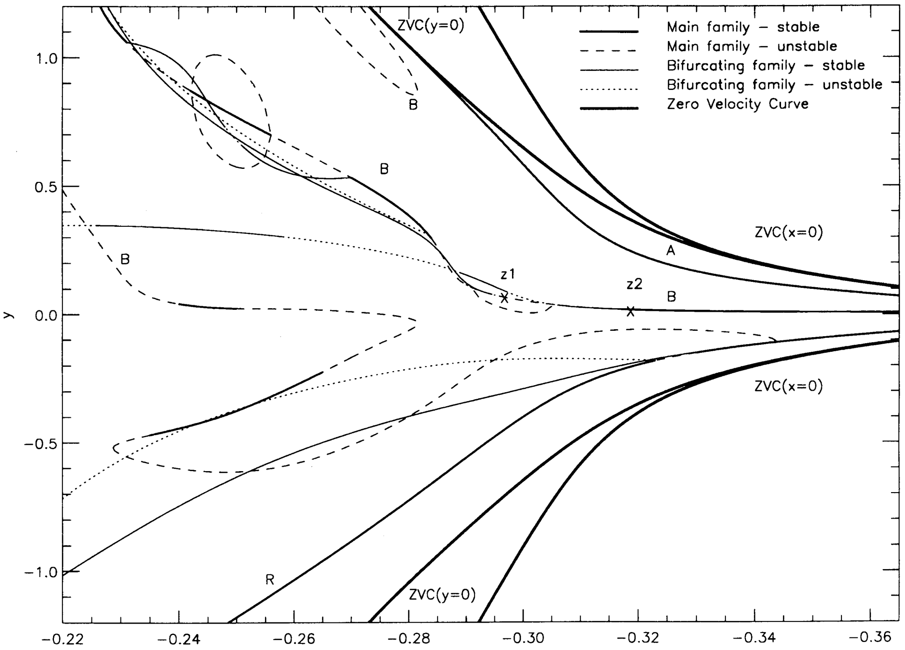

FIG. 4*a*

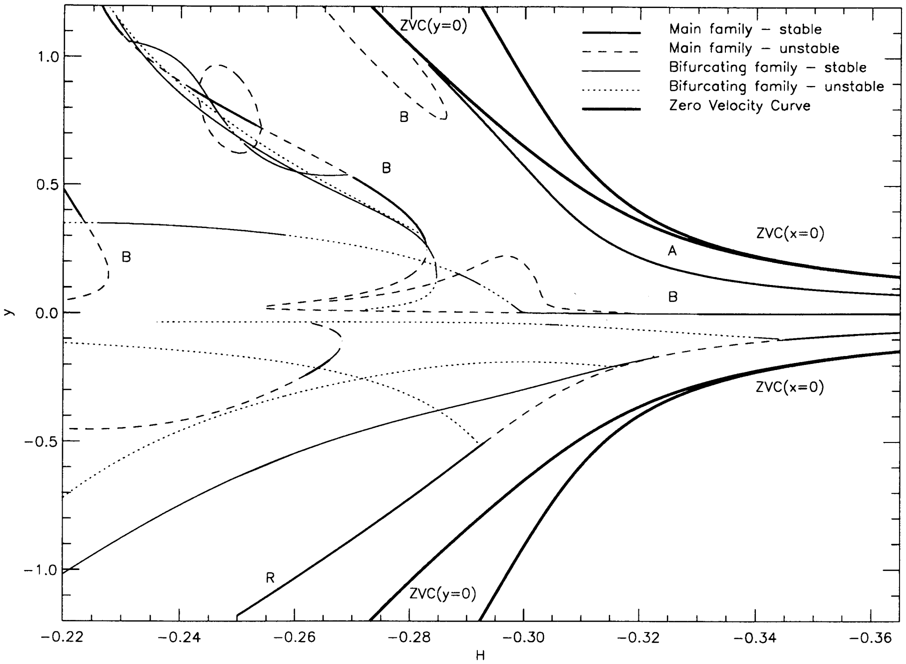

FIG. 4*b*

FIG. 4.—Bifurcation diagrams showing the stable (*solid lines*) and unstable (*broken lines*) regions of the main periodic orbit families and their first-order bifurcations for central mass concentrations (*a*) $B_{\rm cm} = 0.1$, (*b*) $B_{\rm cm} = 0.01$, and (*c*) $B_{\rm cm} = 0.001$.

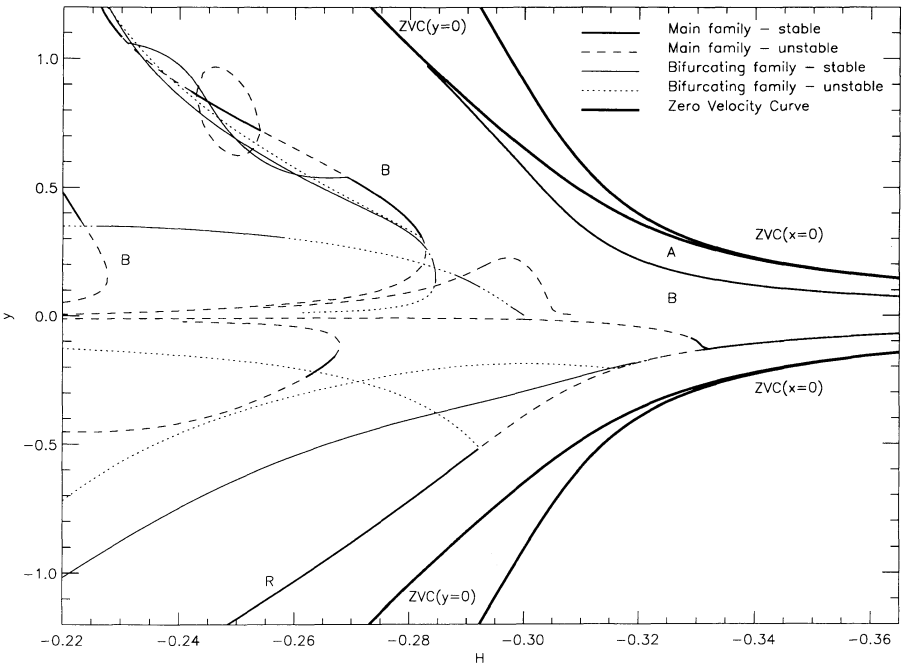

FIG. 4*c*

the retrograde side, bending down at $H = -0.282$, and again bending back up at $H = -0.229$, following an S-shaped path until it joins the main retrograde orbits R at $H = -0.343$. These orbits are mainly unstable with two regions of stability as indicated in Figure 3*a*. Examples of direct orbits along this characteristic are shown in Figure 7*a*, while some retrograde orbits are shown in Figure 7*b*. As concentration of the central mass is increased, this characteristic undergoes significant changes as seen in Figures 3*b* and 3*c*. These orbits do not have an impact on the shape of the galaxy, because they are unstable; their significance lies rather in the set of chaotic orbits starting in the neighborhood of the central mass that they represent.

The retrograde *family R and its bifurcations*.—There is one retrograde family. These orbits are mostly *stable* with regions of *instability between bifurcation points*. They are nearly circu-

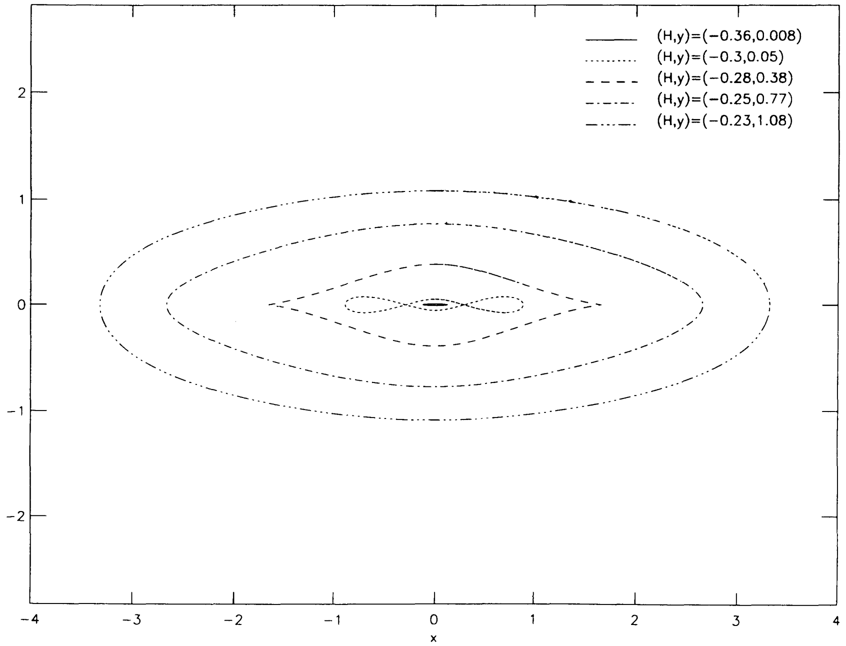

FIG. 5.—Evolution of B orbit family for case I. The starting conditions for each orbit are given in the key at upper right. The innermost orbit, which corresponds to stars in the interior of the potential, is oval and elongated along the major axis of the bar. For larger values of H the orbit develops loops at the ends which open out at still higher H-values, leading again to orbits elongated along the bar.

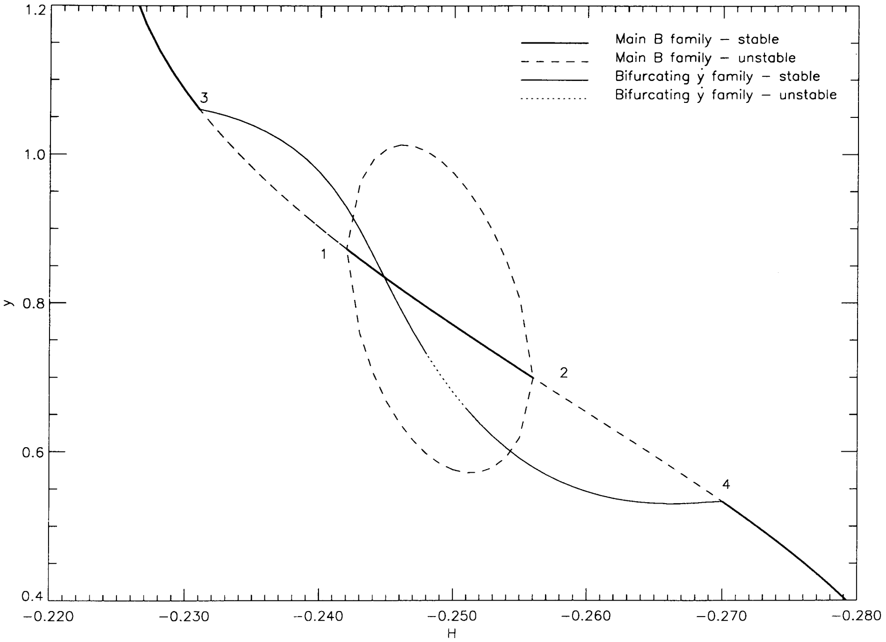

FIG. 6.—Expanded view of the section of the bifurcation diagram for case I containing the y and $\dot{y}$ bifurcations from the direct B family. This section of the diagram is similar for cases II and III. Points of bifurcation in y are indicated by the numerals 1 and 2, while points of bifurcation for the $\dot{y}$ family are indicated by 3 and 4. Stable and unstable parts are indicated by solid and broken lines, respectively.

lar between $H = -0.37$ and $H = -0.3$, after which they start getting elongated along the y-axis until they are oval toward the end of the characteristics.

The only *bifurcation in y* for case I is due to the minor family of orbits already discussed. For case II there are two bifurcation points in $\dot{y}$ (Fig. 3*b*), the orbits along these characteristics being *unstable*, *oval* and elongated along the intermediate axis. For case III there is one bifurcation in y and one in $\dot{y}$ (Fig. 3*c*). The orbits bifurcating in y and $\dot{y}$ are 1:1 and are elongated along the y-axis.

3.2. *Surface of Section*

Surfaces of section (see Binney, Gerhard, & Hut 1985 for an introduction) were computed in the galactic plane for a number of Hamiltonian values for case I, and some of them are collectively plotted in Figure 8. The equations of motion were solved for each Hamiltonian value for particles starting on the positive y-axis with a positive $\dot{x}$ and all other starting values set to zero. Every time the orbit crossed the positive y-axis with a positive $\dot{x}$ a point in the surface of section (or consequent) was obtained.

Surface-of-section plots complement the information obtained from characteristic curves. While the latter give starting conditions for *periodic* orbits, the former show at a galance a cut of the phase space supported by the periodic orbits. A smooth curve, called the invariant curve (IC), formed by consequents represents a stable quasi-periodic orbit, while chaotic orbits are represented by apparently random points in an area bounded by the zero-velocity curve. The right-hand side of the plots in Figure 8 represents the stable direct orbits, while the left-hand side represents the stable retrograde orbits. The invariant curves representing the stable orbits are symmetric in $\dot{y}$. As we go from $H = -0.24$ to $H = -0.34$, the area bounded by the zero-velocity curve, and hence the corresponding surface of section, shrinks in size.

We can see from Figure 3*a* that there are only stable periodic orbits for $H = -0.34$, hence the surface of section at this energy contains smooth curves on both the direct and the retrograde sides. The situation is similar for $H = -0.32$. For $H = -0.3$, the B orbits become unstable and the corresponding invariant curves dissolve. The stable A orbits are represented by the IC near the zero-velocity curve. On the retrograde side we see, in addition to the R orbits, some islands formed by ICs formed near resonances. For $H = -0.28$ we find a small region of stable B orbits and some islands of higher orders of resonances. On the retrograde side we see the appearance of a small IC arising from the minor family already discussed. The main family of B orbits disappear for $H = -0.26$ and $H = -0.24$, although there are still some islands of higher order resonances corresponding to the orbits which bifurcate off the main family in the characteristic diagram.

4. MOTION OUTSIDE THE GALACTIC PLANE

Periodic orbits which have a motion outside the galactic plane are represented in the characteristic diagram by the bifurcations in z and $\dot{z}$ from the main families in the plane. These orbits seem to be more affected by the strength of the central mass than those bifurcating in y or $\dot{y}$ (Figs. 3*a*–3*c*). They are also interesting because they indicate the possibility of the existence of stable three-dimensional orbits which can influence the bulge shape of the galaxy or can attract dissipative gas.

There are two bifurcating z-families, one family bifurcating close to $H = -0.31$ and the other at $H = -0.296$ for case I and close to $H = -0.25$ for the other two cases (the exact points could not be found because of numerical problems). The corresponding (H, z) characteristics are shown in Figure 9. We shall refer to these as families $z1$ and $z2$, respectively. These particular 2:2:1 orbits have been shown (Combes et al. 1990; Pfenniger & Friedli 1991) to be responsible for the box shape

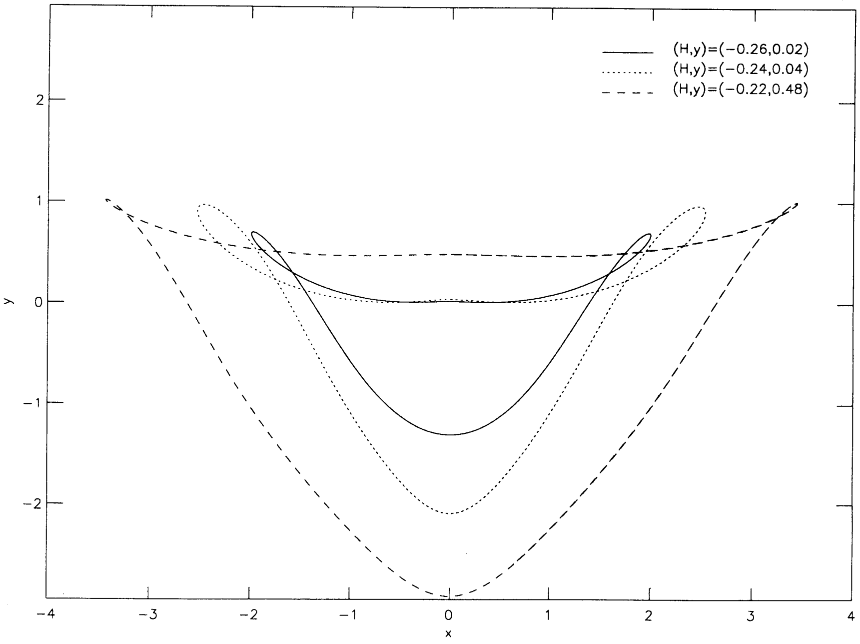

FIG. 7*a*

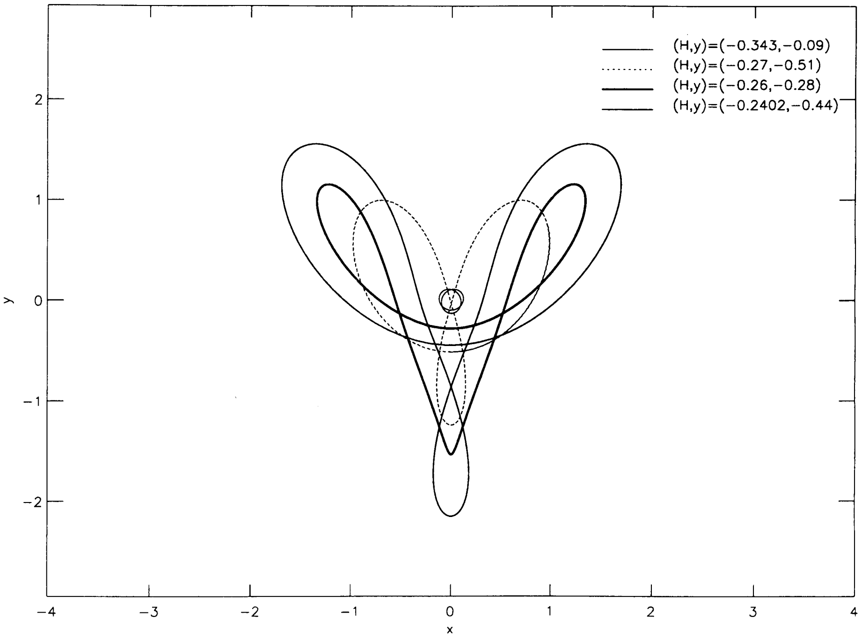

FIG. 7*b*

FIG. 7.—Evolution of minor B orbit family for case I: (*a*) Direct orbits; (*b*) retrograde orbits. The starting conditions for the various orbits are given in the key at upper right. The direct orbits change in size as we go to higher energies, but essentially maintain their shape. The retrograde orbits have three loops which change in size as we move along the orbit characteristic, but otherwise maintain their basic structure.

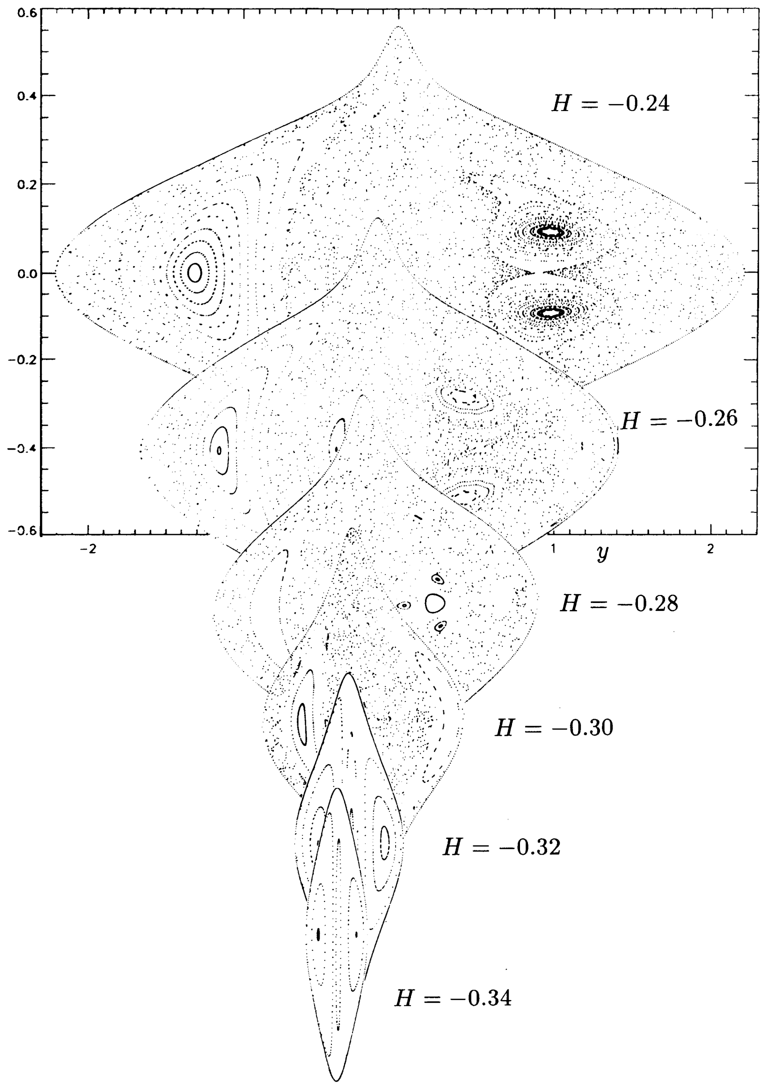

FIG. 8.—Surface-of-section plots for families of orbits in the galactic plane for a series of values of H for case I. Values of $(y, \dot{y})$ for the orbit at the point where it crosses the y-axis with $\dot{x} > 0$ are plotted. Surfaces of section for successive H-values have been plotted on the same scale and are displayed here by overlapping them in such a way that the center of each section is displaced with respect to the previous section by -0.1 in y, while the displacement in $\dot{y}$ varies from -0.4 to -0.2 in steps of -0.05. The main regions of interest are the right-hand sides of the plots, which show the direct orbit families. The invariant curves representing the B family disappear as the value of H increases from $H = -0.32$ to $H = -0.3$.

of typical N-body bars. The stability of these orbits explains why the bending instability observed in N-body simulations (e.g., Raha et al. 1991) saturates at this amplitude and location.

The evolution of the $z1$ *family* in the x-y plane for case I is shown in Figure 10*a*, while Figure 10*b* shows the corresponding motion in the x-z plane. As for the main B family, in the interior of the potential the $z1$ orbits in the x-y plane are elongated along the x-axis and are 2:1 shaped. These loops open out as the value of H increases and the orbits are almost elliptical. For case I the $z1$ family is stable over the entire range of H-values considered. For cases II and III the characteristic is repelled from the interior of the potential for H-values lower than -0.282, and no $z1$ orbits exist below this value. Between $H = -0.25$ and -0.282, unstable $z1$ orbits exist close to the interior of the potential (around $y = 0$ to $y = 0.1$) as indicated in Figures 3*b* and 3*c*, respectively. In the x-y plane they make a figure of 8 about the x-axis at the lower end of the characteristic, while as we move along its parabolic bend they become elliptical with loops at the ends as for case I. The orbits along the stable branch of the characteristic are almost elliptical and elongated along the x-axis as for case I. The motion in the x-z plane indicates that these are not simple tilted orbits.

The evolution of the $z2$ *family* for case I is shown in Figures 11*a* and 11*b*. Interestingly, except for the innermost example shown, this family is unaffected by the strength of the central mass, because it avoids the neighborhood of the central mass. The characteristic is alternatively stable and unstable between H-values: $-0.3 \rightarrow -0.297$(stable) $\rightarrow -0.292$(unstable) $\rightarrow -0.288$(stable) $\rightarrow -0.258$(unstable) $\rightarrow -0.226$(stable) $\rightarrow -0.22$(unstable). As we can see from Figure 11*a*, the innermost orbit in the x-y plane is elliptical with loops at the ends, while as the energy increases the orbits first become elliptical and then gradually become rectangular. In the x-z plane the orbits make two oscillations per turn and so are close to a vertical inner Lindblad resonance. An example of the time evolution of a z-unstable nonperiodic orbit for the potential model of case III is shown in Figure 12. This orbit starts close to the galactic plane in the chaotic region around the horizontal and vertical

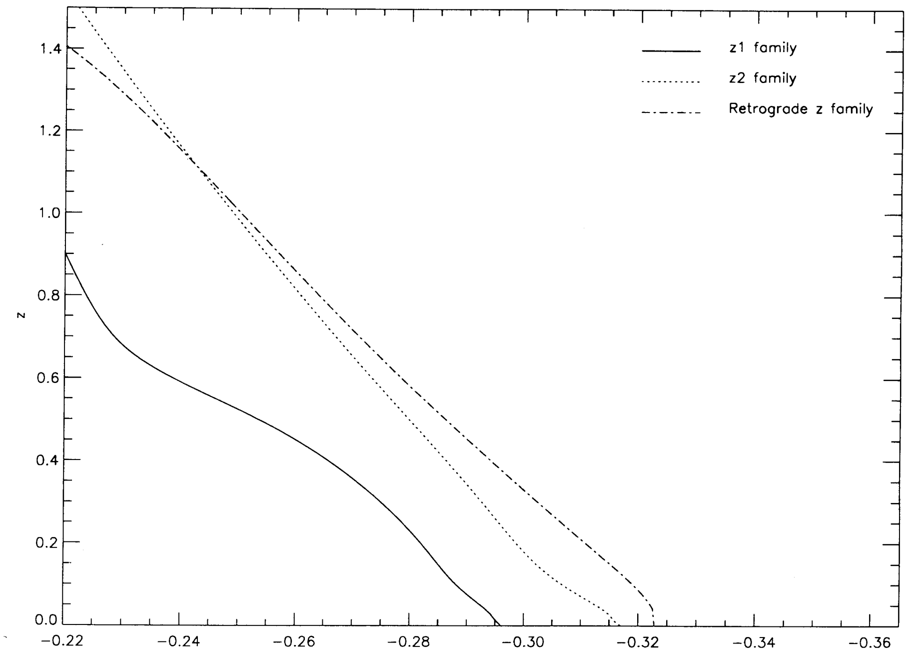

FIG. 9*a*

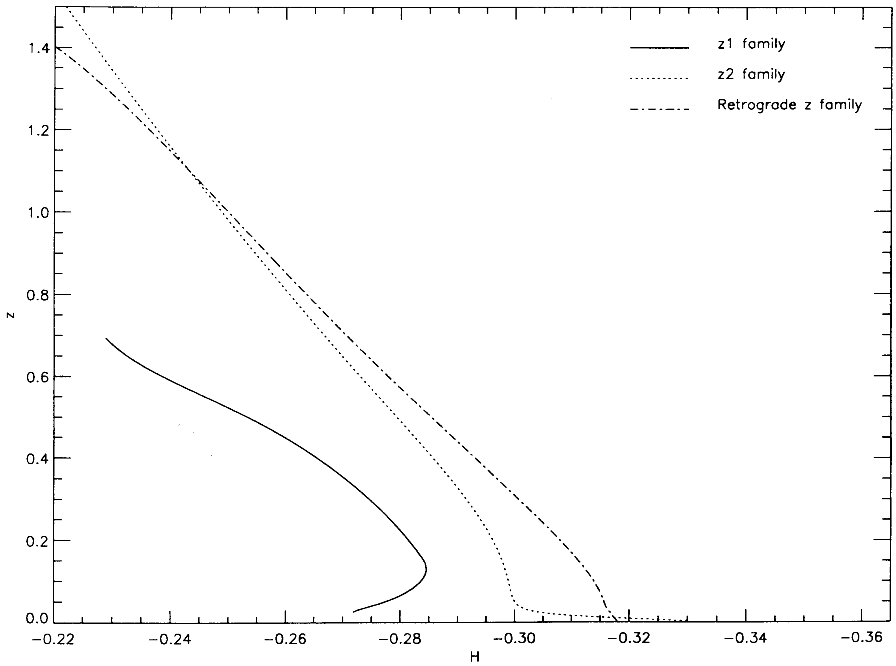

FIG. 9*b*

FIG. 9.—Bifurcation diagrams showing the initial conditions (H_0, z_0) for the *z*1, *z*2, and retrograde *z* families for central mass concentrations (*a*) $B_{\rm cm} = 0.1$, (*b*) $B_{\rm cm} = 0.01$, and (*c*) $B_{\rm cm} = 0.001$. We can see here that as the central mass increases in strength the curves representing the *z*1 orbits bend, reflecting the fact that these orbits take the more energetic stars from the potential interior out of the galactic plane.

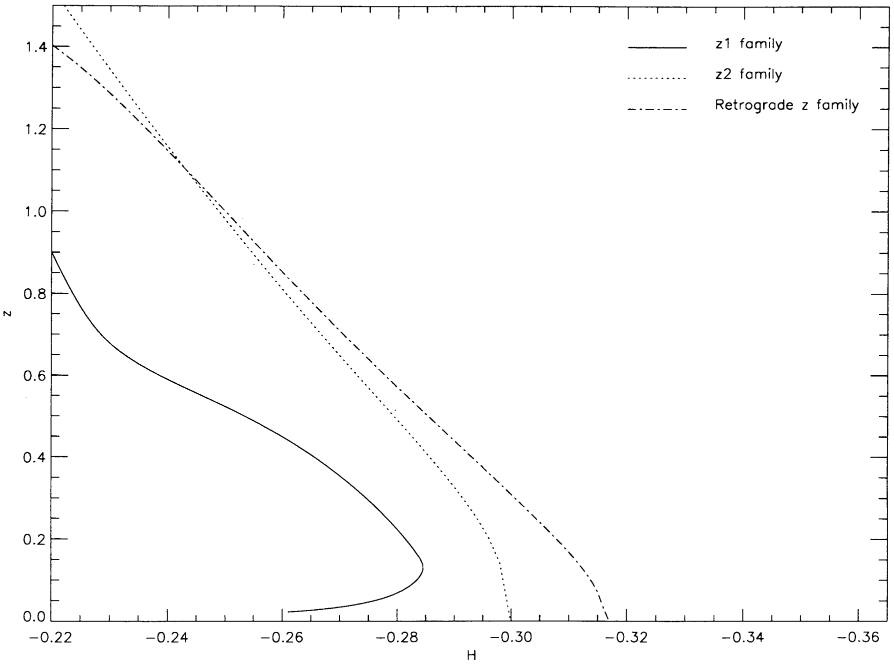

FIG. 9*c*

Lindblad resonances. As is apparent from the diagrams, the orbit soon moves away from the galactic plane, taking stars well out of the plane.

For the retrograde orbits there are *two bifurcations* for case I (z and $\dot{z}$ in Fig. 3*a*). The orbits *bifurcating in z are unstable and nearly circular*, while those *bifurcating in $\dot{z}$ are stable* and *oval* elongated along the y-axis. These are the "anomalous" orbits, but they do not bifurcate from the z-axis as in the study of Heisler, Merritt, & Schwarzschild (1982). This is due to the fact that the radial orbits along the z-axis are completely complex unstable because of the central mass (Martinet & Pfenniger 1987). There is a counterpart of the $\dot{z}$ on the direct side. The orbits are unstable. The corresponding characteristic diagram is shown in Figure 13.

5. SUMMARY OF RESULTS AND DISCUSSION

We have computed characteristic curves for three-dimensional stellar orbits in a barred galaxy with a mass of varying concentration embedded at its center, and have classified the main orbit families. Three different concentrations were considered for the central mass. In each case we found two main families of direct orbits in the equatorial plane (the A family of nearly circular orbits in the potential interior, which become oval and elongated along the bar intermediate axis, and the B family of orbits, which are elongated along the bar major axis and are the most important ones for the bar existence), one of retrograde orbits (these do not play a major role in bar stability), and one minor orbit family. Several bifurcating families, some of which could lead to motion out of the equatorial plane, were found off the main families. The main effect of increasing the strength of the central mass was to destabilize the B orbits in the potential interior. Another orbit family significantly affected was the $z1$ family bifurcating off the B family. This family of stable orbits developed regions of instability in the potential interior.

This study indicates that, as the concentration of the central mass is increased, there will be no stable orbits present in the region where the bar potential competes in strength with the central mass potential, especially around the region of the inner Lindblad resonance. The effective length of the bar reaches a distance of about 4 along the x-axis, as seen in Figure 5 by the B orbits which are sufficiently elongated to support the bar. The ILR, on the other hand, reaches a distance of about 2 along the x-axis, as can be inferred from the bifurcation diagram (Fig. 3*a*). Therefore, increasing the central mass concentration (widening the ILR resonance gap) has an important effect at a distance much larger than the effective central mass radius and about half as large as the bar. A vertical Lindblad resonance is also created by the increase of the central mass. In the region where the central mass successfully competes with the bar (as for the horizontal ILR, this corresponds to a distance of about 2), many stars will leave the plane. This generalizes earlier work (Paper I) in which we considered the problem in two dimensions and were able to predict, based on phase-space volume computations, that above a critical central mass the bar would dissolve. The dissolution of the bar progressively decreases the width of the resonances. Until the bar is completely dissolved, the resonances can act, so their effect is not immediately suppressed.

The fact that the vertical Lindblad resonance occurs nearly in the same energy range as the radial Lindblad resonance is an important aspect of the problem. This coincidence is not fortuitous, since its origin lies in the spherical shape of the central mass potential. From this it follows that the three-dimensional periodic orbits have a banana shape, which in turn influences the three-dimensional shape of the bar. Since this study describes the orbits in a fixed potential, it cannot predict exactly how a global instability will develop, but periodic orbits are essential in complex dynamical systems for explaining why some instabilities can start and where they can saturate. In self-consistent three-dimensional N-body studies

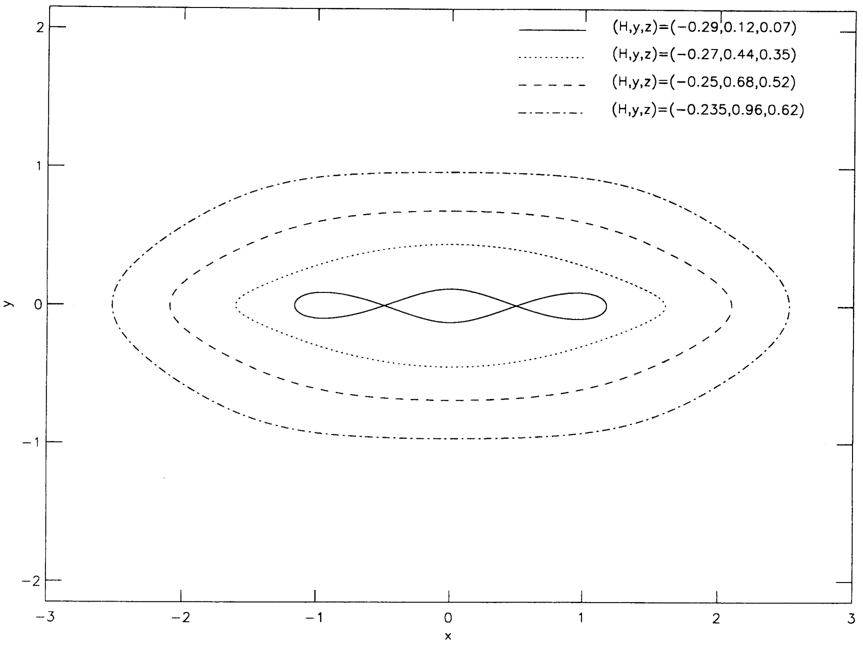

FIG. 10*a*

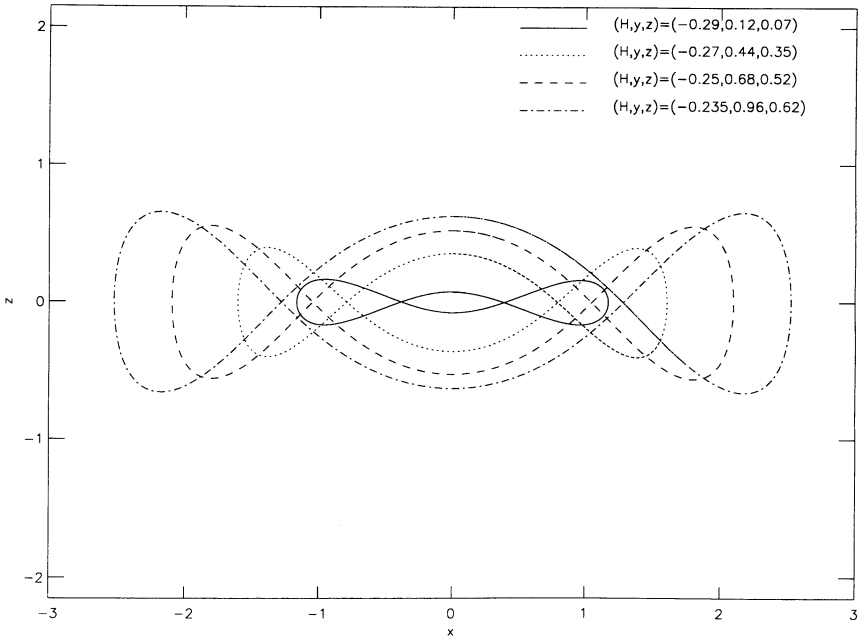

FIG. 10*b*

FIG. 10.—Evolution of $z1$ orbit family for case I: (*a*) x-y projection; (*b*) x-z projection. The starting conditions for the various orbits are given in the key at upper right. The orbits are aligned along the major axis of the bar. In the x-y plane, the innermost orbit has loops at the ends which open out at higher energies. In the x-z plane the orbits have loops at the ends at all the H-values shown here.

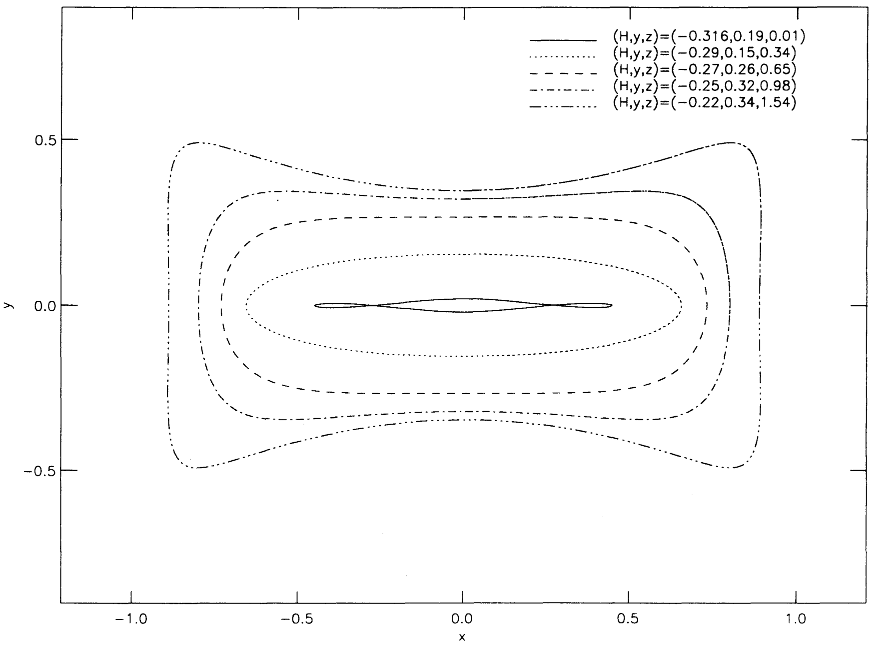

FIG. 11*a*

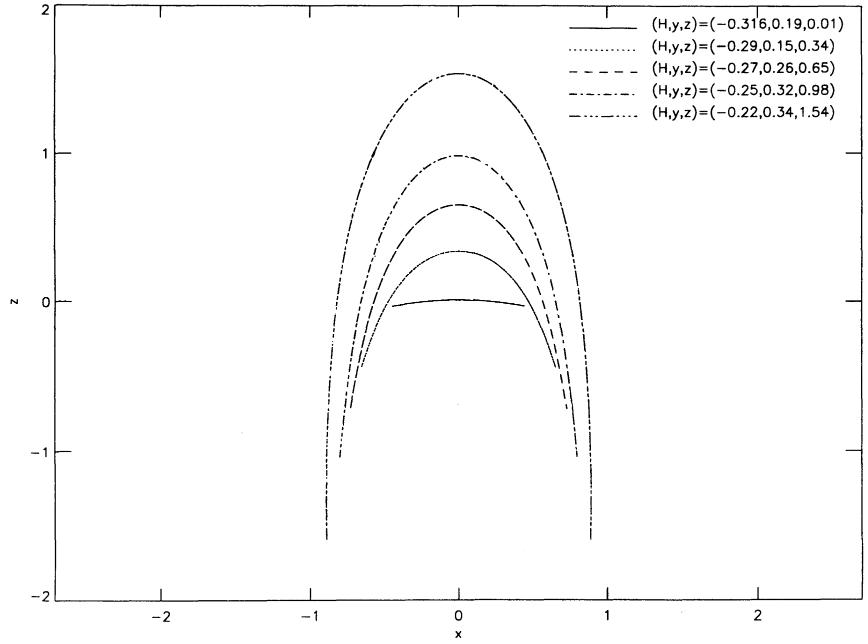

FIG. 11*b*

FIG. 11.—Evolution of $z2$ orbit family for case I: (*a*) x-y projection; (*b*) x-z projection. The starting conditions for the various orbits are given in the key at upper right. In the x-y plane the orbits are aligned along the major axis of the bar. The innermost orbit has loops at the ends which open out as the energy increases, and the orbit gets first oval and then almost rectangular. In the x-z plane the orbits make two oscillations per turn.

stellar bars have been shown to adopt a final peanut shape, precisely because the stable orbits that exist before and after the instability starts are banana-shaped (Combes et al. 1990; Pfenniger & Friedli 1991).

These results are relevant to the study of the structure of galaxies. The slow-feedback effect of bars building up central mass and then dissolving once this mass reaches a critical value is a self-limiting process that may explain why only ~30% of all galaxies are strongly barred. It is interesting to note that from morphological reasoning Kormendy (1979, 1982) has proposed that barred galaxies may in fact dissolve into ovals and lenses. As discussed in § 1, these slow secular processes can be thought of as tending to transform galaxies from one type to another from barred to unbarred and in the direction of increasing the bulge-to-disk ratio.

Many questions concerning the secular evolution of disks remain unanswered. From galaxy catalogs we can infer that disk galaxies are about a third of the time strongly barred, about a third of the time weakly barred, and less than about a third of the time axisymmetric. What is not clearly specified is how frequent the changes are from one type to another, and also what the precise conditions are that could rebuild a bar. Among the weakly barred galaxies, are there features allowing us to distinguish between the bar-forming and the bar-dissolving galaxies? High-resolution N body studies including an adequate description of gas (e.g., Friedli 1992) are required to simulate such possible secular changes properly.

We would like to express our thanks to Ken Freeman, Jerry Sellwood, Françoise Combes, and Lia Athanassoula for stimulating discussions. One of us (H. H.) would like to thank Geneva Observatory for hospitality during the early stages of this work. D. P. is grateful to the Space Telescope Science Institute for hospitality and to the Swiss National Science Foundation for partial support of this work.

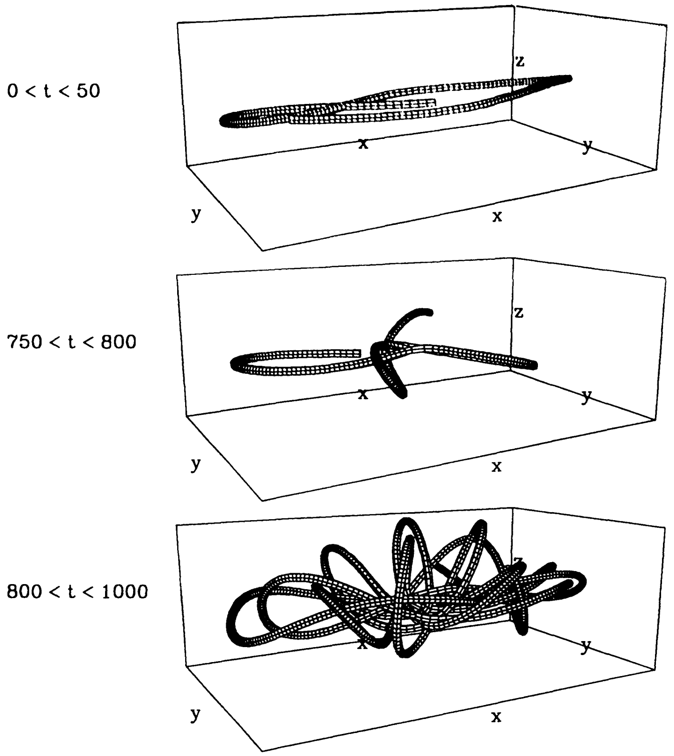

FIG. 12.—Perspective "tube" view of a z-unstable nonperiodic orbit for the model of case III. The orbit starts close to the galactic plane, showing the time evolution in space. The trihedron has the dimensions of the maximal excursions of the orbit in x, y, and z: ± 1.65, ± 1.0, and ± 0.6, respectively. The initial conditions are $x_0 = 0.2$, $y_0 = 0.0$, $z_0 = 0.003$, $\dot{x}_0 = 0.0$, $\dot{y}_0 = 0.37157$, and $\dot{z}_0 = 0.0$ ($H = -0.28$). They correspond to an orbit within the chaotic region around the horizontal and vertical Lindblad resonances. At first ($0 < t < 50$) the trajectory remains close to the plane; it takes amplitude in z (up to ± 0.6 kpc) in the range $750 < t < 800$; and it remains essentially three-dimensional later on ($800 < t$).

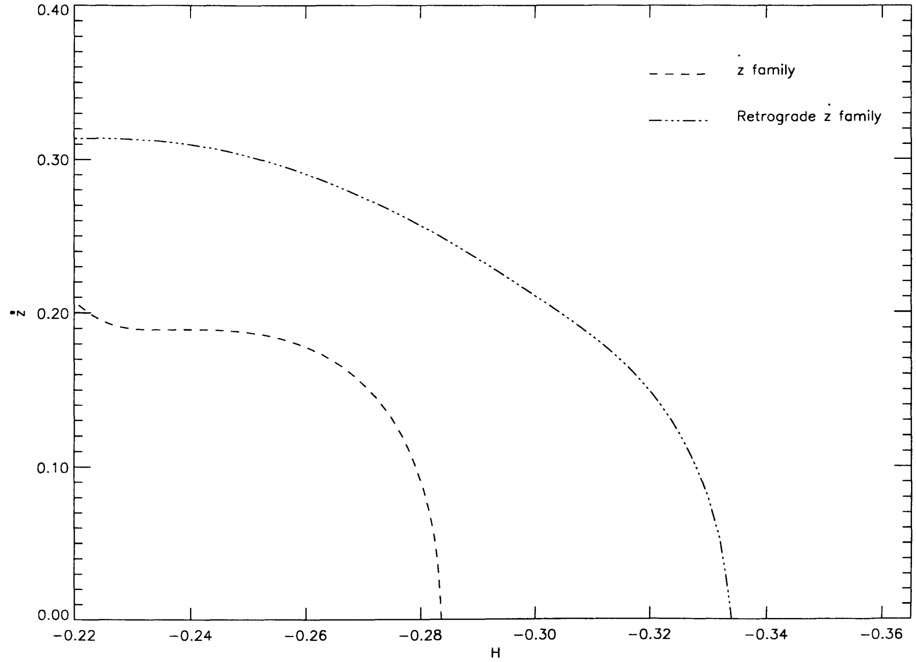

FIG. 13.—Bifurcation diagrams showing the initial conditions $(H_0, \dot{z}_0)$ for the $\dot{z}$ and retrograde $\dot{z}$ families for case I. The corresponding diagrams for the other two cases differ little from this one.

APPENDIX A

COMPUTATION OF POINCARÉ MAPS

An efficient method for computing the intersection of orbits with a surface is necessary to be able to determine not only the location of periodic orbits as described in Appendix B but also the stability of the periodic orbits found. We use a special case of a not widely known but elegant trick due to Hénon (1982), applicable to more general problems than the one discussed here.

Suppose that the system of N differential equations

$$\frac{d\boldsymbol{x}}{dt} = \boldsymbol{F}(\boldsymbol{x}, t) , \qquad \text{where} \qquad \boldsymbol{F} = \{F_1(\boldsymbol{x}), F_2(\boldsymbol{x}), \dots, F_N(\boldsymbol{x})\} , \qquad \boldsymbol{x} = \{x_1, x_2, \dots, x_N\} \tag{A1}$$

is integrated numerically with an adaptive, self-starting integrator for particular initial conditions $\boldsymbol{x}_0$. The specific integrator retained in this paper is a Runge-Kutta-Fehlberg integrator of order 7–8 (RK78) (Fehlberg 1974), satisfying a specified relative error at each time step on each component. Suppose that we want to find the next intersection with the plane $x_N = 0$, with $\dot{x}_N > 0$, where x_N is chosen for convenience as the last component of the vector $\boldsymbol{x}$. First we have to detect between which discrete points $\boldsymbol{x}_i$ the trajectory crosses the plane, which is found by a change of sign along the successive x_{N_i} provided by the integrator. To find the solution exactly at $x_N = 0$, a common method is to interpolate between the $\boldsymbol{x}_i$. This should be done with the same accuracy as provided by the integrator, i.e., a high-order interpolation algorithm should be used. Instead, Hénon propose to make a change of independent variable from t to x_N. The system (A1) becomes

$$\left\{\frac{dx_1}{dx_N} = \frac{F_1}{F_N}, \frac{dx_2}{dx_N} = \frac{F_2}{F_N}, \dots, \frac{dx_{N-1}}{dx_N} = \frac{F_{N-1}}{F_N}, \frac{dt}{dx_N} = \frac{1}{F_N}\right\} . \tag{A2}$$

Starting at $\boldsymbol{x}_i$ (or $\boldsymbol{x}_{i+1}$, whichever is the closest to the plane $x_N = 0$), we solve this new system of N differential equations with the *same* integrator (here RK78), taking as suggested integration "time" step $\Delta x_N = -x_{N_i}$ (or $\Delta x_N = -x_{N_{i+1}}$, respectively). Usually the integrator provides the desired intersection point and intersection time in a single step. Sometimes (e.g., where the orbit is nearly tangent to the section plane) the integrator shortens the suggested step in order to keep the prescribed accuracy, and then a second step is necessary.

To compute a Poincaré "surface" of section (with more than 2 degrees of freedom; more appropriately called a Poincaré map), orbits of a given Hamiltonian H in the plane $x_N = 0$ with a given sign of $\dot{x}_N$ (say $\dot{x}_N > 0$) are computed, and the successive intersections with the plane $x_N = 0$ with the same sign of $\dot{x}_N$ are found with the above method. This defines a discrete map of $N - 2$ variables, since x_N is zero, and a further variable can be eliminated by the integral of motion H. In a Hamiltonian system, one eliminates the conjugate momentum to x_N. We note this map $\boldsymbol{T}_H(\boldsymbol{y})$, where $\boldsymbol{y} = \{x_1, x_2, \dots, x_{N-2}\}$. This map is volume-preserving (see, e.g., Siegel & Moser 1971, § 22) and is a discrete analog of a continuous Hamiltonian system.

APPENDIX B

COMPUTATION OF PERIODIC ORBITS AND THEIR STABILITY INDICES

In a Poincaré map $\boldsymbol{T}_H$, a periodic orbit is a fixed point. So determining a periodic orbit is equivalent to determining the fixed points $\boldsymbol{y}_*$ in the map $\boldsymbol{T}_H$, i.e.,

$$\boldsymbol{T}_H(\boldsymbol{y}_*) = \boldsymbol{y}_* , \qquad \text{where} \qquad \boldsymbol{T}_H = \{T_{H_1}, T_{H_2}, \dots, T_{H_M}\} , \qquad \boldsymbol{y} = \{y_1, y_2, \dots, y_M\} , \tag{B1}$$

or the roots $\boldsymbol{y}_*$ of $\boldsymbol{F}(\boldsymbol{y}) = 0$, where

$$\boldsymbol{F}(\boldsymbol{y}) \equiv \boldsymbol{T}(\boldsymbol{y}) - \boldsymbol{y} . \tag{B2}$$

Multidimensional nonlinear root-finding methods are usually based on Newton's algorithm, where, starting with an initial estimate $\boldsymbol{y}_0$, successive refinements are found by

$$\boldsymbol{y}_{n+1} = \boldsymbol{y}_n - (\nabla \boldsymbol{F})^{-1}(\boldsymbol{y}_n) \cdot \boldsymbol{F}(\boldsymbol{y}_n) . \tag{B3}$$

The iterations are stopped when $\| \boldsymbol{y}_{n+1} - \boldsymbol{y}_n \|$ is sufficiently small. Provided that the Jacobian matrix $\nabla \boldsymbol{F}$ exists and is invertible, this algorithm converges quadratically in the neighborhood of a root; in other words, at each iteration the number of significant digits doubles. One can express $\nabla \boldsymbol{F}$ as $\nabla \boldsymbol{T}_H - \boldsymbol{I}$, where $\boldsymbol{I}$ is the identity matrix. If an invertible matrix $\boldsymbol{S}$ diagonalizes $\nabla \boldsymbol{T}_H$, i.e., $\nabla_H = \boldsymbol{SDS}^{-1}$, where $\boldsymbol{D}$ is a diagonal matrix, then $|\nabla \boldsymbol{F}| = |\boldsymbol{S}||\boldsymbol{D} - \boldsymbol{I}||\boldsymbol{S}|^{-1} = |\boldsymbol{D} - \boldsymbol{I}|$. This determinant is small whenever an eigenvalue of $\nabla \boldsymbol{T}_H$ is close to unity; in this case the inversion of $\nabla \boldsymbol{F}$ is numerically badly conditioned. To avoid round-off errors, we adopt the following approach. Instead of inverting $\nabla \boldsymbol{F}$ in equation (B3), we minimize in the least-squares sense the Euclidean norm

$$\| \nabla \boldsymbol{F}(\boldsymbol{y}_n)(\boldsymbol{y}_{n+1} - \boldsymbol{y}_n) + \boldsymbol{F}(\boldsymbol{y}_n) \| . \tag{B4}$$

For each value $\boldsymbol{y}_n$, we compute $\boldsymbol{F}(\boldsymbol{y}_n)$, $\nabla \boldsymbol{F}(\boldsymbol{y}_n)$, and then solve in the least-squares sense for $\delta \boldsymbol{y} \equiv \boldsymbol{y}_{n+1} - \boldsymbol{y}_n$, from which $\boldsymbol{y}_{n+1} = \delta \boldsymbol{y} + \boldsymbol{y}_n$. We have the robust least-squares algorithm HFTI of Lawson & Hanson (1974), which can handle any degeneracy. Whenever $\nabla \boldsymbol{F}(\boldsymbol{y}_n)$ is degenerate, or is close to being degenerate, it provides among the infinite number of possible solutions $\delta \boldsymbol{y}$ the one which minimizes the Euclidean norm $\| \delta \boldsymbol{y} \|$. Therefore, the differential corrections $\delta \boldsymbol{y}$ are guaranteed not to diverge arbitrarily. If $\nabla \boldsymbol{F}(\boldsymbol{y}_n)$ is invertible, the results of HFTI is equivalent to or better than that of a matrix inversion algorithm.

To compute the Jacobian matrix,

$$\nabla \boldsymbol{T}_H = \begin{pmatrix} \frac{\partial T_{H_1}}{\partial y_1} & \frac{\partial T_{H_1}}{\partial y_2} & \cdots & \frac{\partial T_{H_1}}{\partial y_M} \\ \frac{\partial T_{H_2}}{\partial y_1} & \frac{\partial T_{H_2}}{\partial y_2} & \cdots & \frac{\partial T_{H_2}}{\partial y_M} \\ \vdots & \vdots & \ddots & \vdots \\ \frac{\partial T_{H_M}}{\partial y_1} & \frac{\partial T_{H_M}}{\partial y_2} & \cdots & \frac{\partial T_{H_M}}{\partial y_M} \end{pmatrix}, \tag{B5}$$

we approximate it by finite differencing, i.e., at each iteration,

$$\frac{\partial \boldsymbol{T}_H}{\partial y_i} = \frac{\boldsymbol{T}_H(\{y_1, y_2, \ldots, y_i + \Delta y_i, \ldots, y_M\}) - \boldsymbol{T}_H(\boldsymbol{y})}{\Delta y_i} + O(\Delta y_i) . \tag{B6}$$

So computing the Jacobian requires at least computing the map $\boldsymbol{T}_H$ $M + 1$ times. For particularly unsuitable orbits one computes

$$\frac{\partial \boldsymbol{T}_H}{\partial y_i} = \frac{\boldsymbol{T}_H(\{y_1, y_2, \ldots, y_i + \Delta y_i, \ldots, y_M\}) - \boldsymbol{T}_H(\{y_1, y_2, \ldots, y_i - \Delta y_i, \ldots, y_M\})}{2\Delta y_i} + O(\Delta y_i^2) . \tag{B7}$$

This alternative approximation is more precise than the previous one (eq. [B6]) but requires $2M + 1$ evaluations of $\boldsymbol{T}_H$.

In symmetric potentials many periodic orbits have some degree of symmetry, and it is not necessary always to search the roots over all the coordinates. The program used in this paper allows us to choose any combination of variable and fixed coordinates. In this case the Jacobian and the least-squares evaluation are computed only for the variable coordinates. This speeds up the finding of periodic orbits correspondingly.

When a periodic orbit $\boldsymbol{y}_*$ is found, the Jacobian $\nabla \boldsymbol{T}_H(\boldsymbol{y}_*)$ calculated for all the M coordinates is also the linear approximation of the map phase space around y_*, since

$$\boldsymbol{T}_H(\boldsymbol{y}_* + \Delta \boldsymbol{y}) = \boldsymbol{T}_H(\boldsymbol{y}_*) + \nabla \boldsymbol{T}_H(\boldsymbol{y}_*) \cdot \Delta \boldsymbol{y} + O(\|\Delta \boldsymbol{y}\|^2) . \tag{B8}$$

In this paper the potentials are three-dimensional, so phase space has six dimensions, and the map $\boldsymbol{T}_H$ has four dimensions. The four eigenvalues of $\nabla \boldsymbol{T}_H(\boldsymbol{y}_*)$ can easily be computed, owing to its special Hamiltonian (or symplectic) structure (see, e.g., Siegel & Moser 1971; Pfenniger 1987). If we note a_{ij} the elements of the matrix $\nabla \boldsymbol{T}_H(\boldsymbol{y}_*)$, then the characteristic polynomial has the form

$$\lambda^4 + \alpha\lambda^3 + \beta\lambda^2 + \alpha\lambda + 1 = 0 , \tag{B9}$$

where

$$\alpha = -\sum_{i=1}^{4} a_{ii} , \qquad \beta = \sum_{i=1}^{3} \sum_{j=i+1}^{4} a_{ii} a_{jj} - a_{oj} a_{ji} . \tag{B10}$$

To solve the quartic (B9), it is convenient to compute the following quantities:

$$\Delta = \alpha^2 - 4\beta + 8 , \qquad b_1 = -\tfrac{1}{2}(\alpha + \sqrt{\Delta}) , \qquad b_2 = -\tfrac{1}{2}(a - \sqrt{\Delta}) . \tag{B11}$$

The coefficients b_i appear when equation (B9) is rewritten as

$$(\lambda^2 + b_1 \lambda + 1)(\lambda^2 + b_2 \lambda + 1) = 0 . \tag{B12}$$

It follows that the eigenvalues λ_i are the roots of $\lambda^2 + b_1 \lambda + 1 = 0$ and $\lambda^2 + b_2 \lambda + 1 = 0$.

Following the position of the eigenvalues in the complex plane, the motion around a periodic orbit can have seven distinct qualitative behaviors (Broucke 1969).

1. The periodic orbit is *stable* if the eigenvalues form two pairs of complex conjugate eigenvalues of modulus 1 in the form $\{\lambda, \bar{\lambda}, \mu, \bar{\mu}\}, |\lambda| = 1, |\mu| = 1$. In this case $\Delta \geq 0$ and $|b_i| \leq 2$. Neighboring trajectories rotate around the periodic orbit, i.e., they are quasi-periodic.
2. The periodic orbit is *complex unstable* if the four eigenvalues form a quadruplet of pairs of reciprocal and conjugate complex numbers not on the unit circle, in the form $\{\lambda, \bar{\lambda}, 1/\lambda, 1/\bar{\lambda}\}, |\lambda| \neq 1$. In this case $\Delta < 0$. Neighboring trajectories simultaneously rotate and diverge exponentially from the periodic orbit.
3. The periodic orbit is *even semiunstable* if one pair of distinct eigenvalues is real and positive and the other pair is on the unit circle, in the form $\{\lambda, 1/\lambda, \mu, \bar{\mu}\}, \lambda > 1, |\mu| = 1$. Neighboring orbits diverge exponentially in one direction.
4. The periodic orbit is *odd semiunstable* if one pair of distinct eigenvalues is real and negative and the other pair is on the unit circle, in the form $\{\lambda, 1/\lambda, \mu, \bar{\mu}\}, \lambda < -1, |\mu| = 1$. Neighboring orbits diverge exponentially in one direction. The difference with the previous case is that the diverging consequences in a Poincaré may appear alternatively on both sides of the direction of instability.

5. The periodic orbit is *even-even unstable* if two pairs of distinct eigenvalues are real and positive in the form $\{\lambda, 1/\lambda, \mu, 1/\mu\}$, $\lambda > 1, \mu > 1$. Neighboring orbits diverge exponentially in two directions.
6. The periodic orbit is *odd-odd unstable* if two pairs of distinct eigenvalues are real and negative in the form $\{\lambda, 1/\lambda, \mu, 1/\mu\}$, $\lambda < -1, \mu < -1$. Neighboring orbits diverge exponentially in two directions.
7. Finally, the periodic orbit is *even-odd unstable* if two pairs of distinct eigenvalues are real, one positive and one negative, in the form $\{\lambda, 1/\lambda, \mu, 1/\mu\}, \lambda > 1, \mu < -1$.

REFERENCES

Athanassoula, E., Bienaymé, O., Martinet, L., & Pfenniger, D. 1983, A&A, 127, 349
Bettoni, D., & Galletta, G. 1991, in Dynamics of Disc Galaxies, ed. B. Sundelius (Göteborg: Göteborg Univ. and Chalmers Univ. of Technol.), 317
Binney, J. J., Gerhard, O. E., & Hut, P. 1985, MNRAS, 215, 59
Broucke, R. 1969, Am. Inst. Aeronautics Astronautics J., 7 (No. 6), 1003
Combes, F., Debbasch, F., Friedli, D., & Pfenniger, D. 1990, A&A, 233, 82
Combes, F., & Sanders, R. H. 1981, A&A, 96, 194
Contopoulos, G. 1986, Celest. Mech., 38, 1
Contopoulos, G., & Magnenat, P. 1985, Celest. Mech. 37, 387
Contopoulos, G., & Papayannopoulos, T. 1980, A&A, 92, 33
Fehlberg, E. 1974, Classical Fifth-, Sixth-, Seventh- and Eighth-Order Runge-Kutta Formulae with Stepsize Control (NASA TR 287)
Friedli, D. 1992, Ph.D. thesis, Univ. Geneva
Friedli, D., & Benz, W. 1993, A&A, in press
Friedli, D., Benz, W., & Martinet, L. 1991, in Dynamics of Disc Galaxies, ed. B. Sundelius (Göteborg: Göteborg Univ. and Chalmers Univ. of Technol.), 181
Frogel, J. A. 1988, ARA&A, 26, 51
Gilmore, G., Wyse, R. F. G., & Kuijken, K. 1990, ARA&A, 27, 555
Gurzadayan, V. G., & Savvidy, G. K. 1986, A&A, 160, 203
Habing, H. J., Olnon, F. M., Chester, T., Gillett, F., Rowan-Robinson, M., & Neugebauer, G. 1985, A&A, 152, L1
Hasan, H., & Norman, C. A. 1990, ApJ, 361, 69 (Paper I)
Hayakawa, S., Matsumoto, T., Murakami, H., Uyama, K., Thomas, J. A., & Yamagami, T. 1981, A&A, 100, 116
Heisler, J., Merritt, D., & Schwarzschild, M. 1982, ApJ, 258, 490
Hénon, M. 1965, Ann. d'Astrophys., 28, 992
———. 1982, Physica, D, 5, 412
Kent, S. M., Mink, D., Fazio, G., Koch, D., Melnick, G., Tardiff, A., & Maxson, C. 1992, ApJS, 78, 403
Kormendy, J. 1979, ApJ, 227, 714
———. 1982, in Morphology and Dynamics of Galaxies, ed. L. Martinet & M. Mayor (Geneva: Geneva Observatory), 115
Lawson, C. L., & Hanson, R. J. 1974, Solving Least Squares Problems (Englewood Ciffs: Prentice-Hall)
Magnenat, P. 1982, A&A, 108, 89
Martinet, L., & Pfenniger, D. 1987, A&A, 173, 81
Martinet, L., & Udry, S. 1990, A&A, 235, 69
Miralda-Escudé, J., & Schwarzschild, M. 1989, ApJ, 339, 752
Mould, J. 1986, in Stellar Populations, ed. C. A. Norman, A. Renzini, & M. Tosi (Cambridge: Cambridge Univ. Press), 9
Petrou, M. 1984, MNRAS, 211, 1P
Pfenniger, D. 1984a, A&A, 134, 384
———. 1984b, A&A, 141, 171
———. 1985, A&A, 150, 112
———. 1987, A&A, 180, 79
———. 1991, in Dynamics of Disc Galaxies, ed. B. Sundelius (Göteborg: Göteborg Univ. and Chalmers Univ. of Technol.), 191
———. 1992, in Evolution of Interstellar Matter and Dynamics of Galaxies, ed. J. Palouš (Cambridge: Cambridge Univ. Press), 328
———. 1993, in Proc. 12th Moriond Astrophysics Meeting, Physics of Nearby Galaxies: Nature or Nurture? ed. T. X. Thuan, C. Balowski, & J. T. T. Vân (Gif-sur-Yvette: Editons Frontières), in press
Pfenniger, D., & Friedli, D. 1991, A&A, 252, 75
Pfenniger, D., & Norman, C. 1990, ApJ, 363, 391
Raha, N., Sellwood, J. A., James, R. A., & Kahn, F. D. 1991, Nature, 352, 411
Rich, R. M. 1989, AJ, 95, 828
Schwarzschild, M. 1979, ApJ, 232, 236
———. 1982, ApJ, 263, 599
Siegel, C. L., & Moser, J. K. 1971, Lectures on Celestial Mechanics (Berlin: Springer)
Sparke, L., & Sellwood, J. A. 1987, MNRAS, 225, 653
Teuben, P., & Sanders, R. 1985, MNRAS, 212, 257
Udry, S. 1991, A&A, 245, 99
Wielen, R. 1977, A&A, 60, 623